# Neuronal Spatial Arrangement Shapes Effective Connectivity Traits of *in vitro* Cortical Networks

Elisenda Tibau, Adriaan-Alexander Ludl, Sten Rüdiger, Javier G. Orlandi, and Jordi Soriano

**Abstract**—We studied effective connectivity in rat cortical cultures with various degrees of spatial aggregation, ranging from homogeneous networks to highly aggregated ones. We considered small cultures $3$ mm in diameter and that contained about $2{,}000$ neurons. Spatial inhomogeneity favored an increase of metric correlations and connectivity among neighboring neurons. Effective connectivity was determined from spontaneous activity recordings using calcium fluorescence imaging. We used generalized transfer entropy as tool to infer the effective connectivity. We carried out numerical simulations to build networks that mimicked the experimental ones and to test the reliability of the connectivity–inference algorithm. Effective connectivity traits were investigated during the development of the cultures over two weeks, and along the gradual blockade of excitatory connections through CNQX. We observed that the average effective connectivity rapidly increased during culture development. At day *in vitro* (DIV) 15 the average excitatory in–degree was measured as $\bar{k}_E^{\text{in}} \simeq 50$ for homogeneous and semi aggregated networks, and $\bar{k}_E^{\text{in}} \simeq 120$ for aggregated ones, and with 20 percent inhibition. Aggregated cultures exhibited assortative traits and a high resilience to chemical damage, while the other cultures were dissassortative or neutral, and less resilient. Our work illustrates the role of metric correlations in spatially embedded networks in shaping connectivity and activity traits in living neuronal networks.

**Index Terms**—Neuronal cultures, spatial networks, calcium fluorescence imaging, generalized transfer entropy, effective connectivity

## 1 Introduction

One of the most exciting research goals in modern neuroscience is the understanding of the relationship between structural and effective connectivity [1], [2]. The physical wiring among neurons together with their dynamics give rise to a rich activity repertoire that requires complex analyses and modeling to be understood. While the structural connectivity is relatively hardwired, the effective one may substantially vary depending on the number of dynamic elements in action and the paths along which information flows. Additionally, living neuronal networks may show two distinct effective connectivity patterns, one associated to the spontaneous activity of the network and another one associated to evoked or task–related activity.

The assessment of key structural connectivity features from activity data is a complex inverse problem that requires the association of firing patterns among neurons with specific structural connections. This difficulty has fostered the continuous development of new methods, their test through numerical simulations, and their implementation in experimental data [2], [3], [4].

- *E. Tibau, A.-A. Ludl, and J. Soriano are with Universitat de Barcelona, Universitat de Barcelona Institute of Complex Systems (UBICS), Barcelona 08028, Spain. E-mail: elisenda.tibau@gmail.com, adriaan.ludl@fmc.ub.edu, jordi.soriano@ub.edu.*
- *S. Rüdiger is with the Humboldt Universität zu Berlin, Berlin 10099, Germany. E-mail: sten.ruediger@physik.hu-berlin.de.*
- *J. G. Orlandi is with the University of Calgary, Calgary, AB T2N 1N4, Canada. E-mail: javier.orlandigomez@ucalgary.ca.*

*Manuscript received 1 Jan. 2018; revised 7 June 2018; accepted 25 July 2018. Date of publication 3 Aug. 2018; date of current version 5 Mar. 2020. (Corresponding author: Jordi Soriano.) Recommended for acceptance by G. Yan. Digital Object Identifier no. 10.1109/TNSE.2018.2862919*

In particular, the use of small living neuronal networks as laboratories for connectivity studies has gained substantial attention. Two technologies to monitor activity in these living systems have become central, namely *calcium fluorescence imaging* [5], [6], [7], [8], [9] and *multi–electrode arrays* (MEAs) [10], [11], [12], [13], [14], [15]. The interest of these studies is not only to quantify the mechanisms shaping neuron–to–neuron interactions, but also to understand up to which extent the inferred effective connectivity captures crucial aspects of the network's structural blueprint.

Neuronal cultures, i.e., dissociated neurons grown *in vitro* [7], [10], [16], are among the most attractive small living systems for effective connectivity studies [3], [4], [13]. Their accessibility and ease manipulation allow for a variety of preparations, from relatively simple homogeneous neuronal assemblies to intricate bioengineered designs [17]. Neuronal cultures are also ideally suited to study the role of spatial embedding and metric correlations in the formation, structure and dynamics of neuronal circuits [18], [19], [20]. Indeed, the analysis of spatial networks [21] has provided valuable insight in fields as diverse as transportation or epidemics [21], [22], [23], but it has been relatively poorly explored in the context of neuronal circuits. The problem of spatial embedding in neuroscience is central since all living neuronal systems are embedded in a physical space [24]. The embedding constrains the layout of network connectivity, either by guiding connections or by restraining them.

In this work we investigated effective connectivity by exploring, both numerically and experimentally, spatial networks in which we adjusted the spatial arrangement of the neurons by tuning their degree of aggregation. The simulated networks were used to select the most appropriate

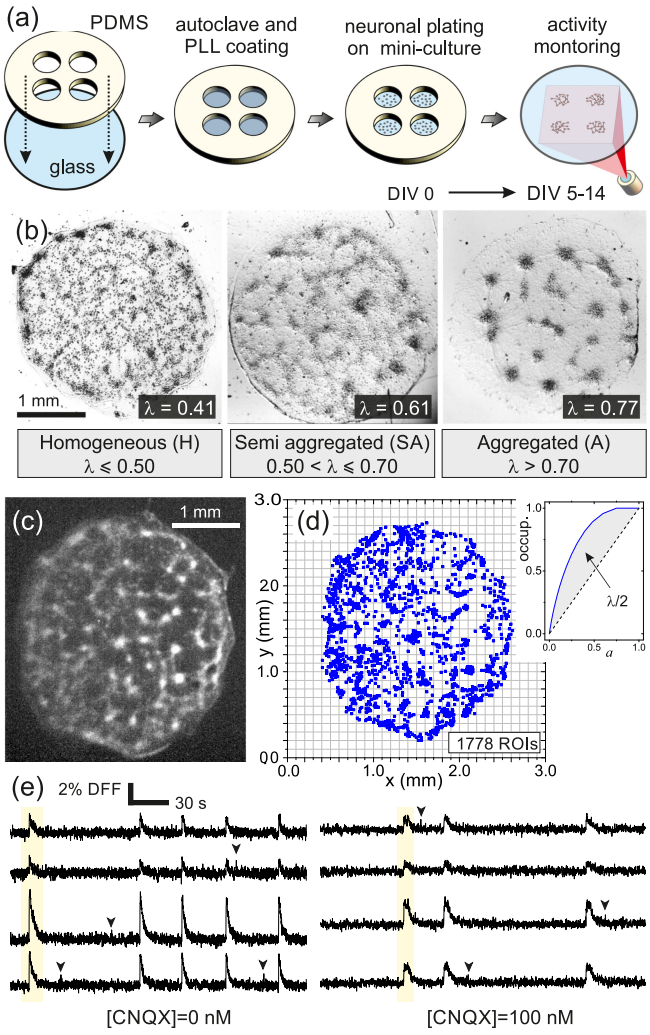


Fig. 1. *Preparation and analysis of neuronal cultures.* (a) Sketch of the preparation of 4 mini cultures for imaging. (b) Examples of neuronal cultures with gradually higher degree of aggregation $\lambda$. For small $\lambda$ single neurons are visible (small dark features). For large $\lambda$ neurons form dense aggregates. Cultures are classified as Homogeneous (H), Semi aggregated (SA) or Aggregated (A) according to their $\lambda$ value. (c) Integrated fluorescence image of spontaneous activity in a SA culture. Bright objects are firing neurons. (d) Corresponding Regions of Interest (ROIs) from which fluorescence time series are extracted. The grey grid is used to compute the Lorenz curve and extract the value of $\lambda \simeq 0.59$ (inset). (e) Examples of fluorescence time series. The traces are grouped according to two different pharmacological conditions, and correspond to the same neurons on each line. Yellow boxes highlight network bursts; arrow heads mark firing events outside bursting episodes. The signal–to–noise ratio of the traces is $\mathrm{SNR} \simeq 5$. %DFF indicates the relative increase in fluorescence.

connectivity–inference algorithm and to complement the experimental observations. Experiments were then analyzed with the selected tool, and network theory was applied to the data in order to identify hallmarks of effective connectivity which can be ascribed to the imposed physical construction.

## 2 Experimental Results: Overview

We considered small cultures of primary cortical neurons grown on 3 mm diameter circular wells (*mini cultures*) that contained $N \simeq 2{,}000$ neurons (see Methods and Fig. 1). The advantage of these mini cultures is that the number of neurons is sufficiently high for the network to show rich collective behavior—in the form of spontaneous activity—and sufficiently small for the data to be numerically tractable.

These cultures were tuned to exhibit different spatial arrangements of the neurons on the substrate, from homogeneous configurations to highly aggregated ones, with the latter consisting of *islands* of highly packed neurons. This spatial distribution of the cultured neurons was quantified through the aggregation coefficient $\lambda$ (Fig. 1b). We used calcium fluorescence imaging to monitor spontaneous activity. An experiment could involve several recordings, which were acquired at 45 frames per second (fps) along 10–30 min. Firing neurons were identified as bright spots on the images, and associated to regions of interest from which fluorescence times series were extracted (Figs. 1c, 1d, and 1e).

Two groups of experiments were performed, *development* and *connectivity weakening*. For the former, we monitored spontaneous activity as the cultures matured, typically from day *in vitro* (DIV) 5 to 16. For the latter, we considered mature cultures at around DIV 14 and monitored their spontaneous activity as the connectivity strength among excitatory neurons was gradually reduced with the AMPA–receptor antagonist CNQX. In either case, neuronal network activity was characterized by periodic episodes of high coherence (*network bursts*) in which most of the neurons fired together in a short time window [Fig. 1e] combined with intervals of sporadic firing. Effective connectivity was inferred from the activity data and diverse network measures were evaluated.

## 3 Numerical Results

### 3.1 Simulation of Spatial Networks

To complement experimental observations, we simulated *directed* spatial networks of 2,000 neurons placed in a circular area 3 mm in diameter, and distributed either in a homogeneous or in an aggregated manner. As in the experiments, aggregation resulted in the concentration of neurons in small islands (Fig. 2). The metric construction of the network favored distinct connectivity layouts. Neurons in the homogeneous case effectually connected to any other neuron in a broad neighborhood, leading to networks that mimicked the characteristics of *geometric* random graphs [18]. By contrast, neurons in the aggregated case preferentially connected within their island, leading to networks with high locality and modular characteristics, as shown in the Supplemental Material (SM), Fig. S1, which can be found on the Computer Society Digital Library at http://doi.ieeecomputersociety.org/10.1109/TNSE.2018.2862919.

A comparison of the connectivity traits between the two network constructions revealed further differences (Figs. 2e and 2f). The distributions of clustering coefficients CC, in-degrees $k^{\mathrm{in}}$ and out–degrees $k^{\mathrm{out}}$ for the homogeneous network were more symmetric and narrower than for the aggregated network. The islands of high neuronal density of the latter favored much higher CC and connectivity values. Interestingly, the distribution of CC values for the homogeneous network markedly differed from an Erdös–Rény (ER) random graph, i.e., a space–free network (see SM, Fig. S2, available online). Values of $\mathrm{CC} \simeq 0$ in the simulated networks signaled the presence of sparsely connected neurons. Thus, a heterogeneous connectivity emerged despite

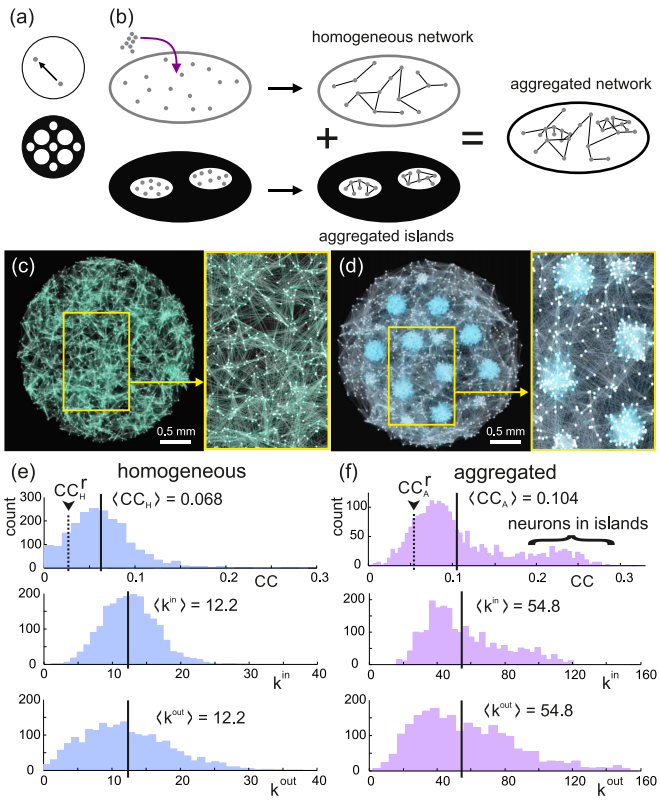


Fig. 2. *In silico networks.* (a) Construction of the networks. Two color patterns were used to direct neuronal growth: homogeneous (top) and patterned substrate (bottom) for aggregated networks. Neurons grow only in the white areas. (b) An aggregated network is built as juxtaposition of homogeneous networks. (c)–(d) Overview of homogeneous (c) and aggregated (d) networks with their corresponding details. $N = 2{,}000$ neurons in both cases. Drawn using Gephi [25]. (e)–(f) Distributions of major connectivity traits for the two configurations, namely clustering coefficient (CC), in–degree $k^{\text{in}}$ and out–degree $k^{\text{out}}$. Solid lines show the average values. Dashed lines with arrow heads indicate the corresponding average CC values for an equivalent ER random graph with average connectivity $\bar{k} = \langle k^{\text{in}} + k^{\text{out}} \rangle_N$, $N = 2{,}300$ neurons, and computed as $\text{CC}^r = \bar{k}/N$. $\text{CC}^r_H = 0.012$, $\text{CC}^r_A = 0.055$.

homogeneity in the distribution of neurons, and illustrates the impact of metric correlations in shaping connectivity.

Simulated spontaneous activity of these networks qualitatively reproduced the experimental observations. Quasi–periodic, whole population network bursts were observed in all spatial configurations, although the aggregated case required higher connectivity strengths for coherent firing (see SM, Fig. S3, available online). The similarity in the dynamics was due to the small size of the cultures in comparison to the axonal length and that favored a broad network interconnectivity, both between neurons and aggregates [19]. Only in the case of extreme aggregation coherent collective dynamics was replaced by fragmented, local activity [26].

By gradually reducing the excitatory connectivity strength $g_{\text{AMPA}}$ we could simulate the effect of CNQX (see SM, Fig. S3, available online). We again observed similar results as in the experiments, with a typical firing frequency of 3 bursts/min in the unperturbed case that progressively decayed as $g_{\text{AMPA}}$ decreased. Coherent activity in homogeneous networks stopped abruptly for a critical connectivity strength, while in aggregated networks activity gradually split into independent groups of aggregates.

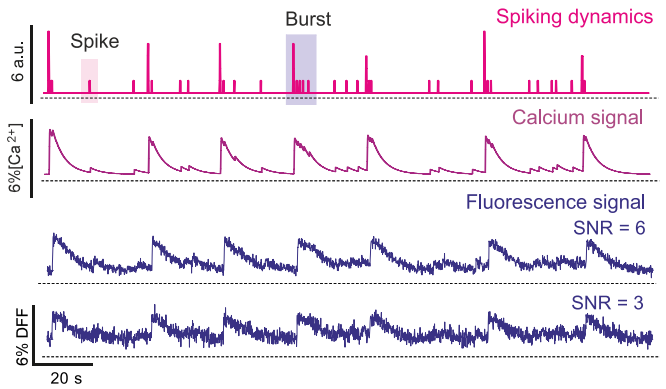


Fig. 3. *Dynamics of simulated networks.* From top to bottom, simulated activity of a single regular spiking neuron together with its calcium and fluorescence signals, and for two SNRs of fluorescence.

### 3.2 Selection of the Reconstruction Method

Given the appropriateness of our *in silico* networks to reproduce the dynamics of neuronal cultures, we used them to test the validity of different connectivity inference algorithms. For simplicity we considered 1,000 neurons in a homogeneous configuration, and simulated their dynamics for 10 min. Spike trains were then converted into noisy calcium fluorescence time series that mimicked the experimental data (see Methods and Fig. 3).

We organized the analysis of the numerical results in two groups. In the first one, the binary firing sequence of each neuron was sampled with a fixed signal–to–noise (SNR) ratio and two different frame rates (fps). In the second one, data was sampled at 50 fps but with two contrasting SNRs. In both groups, connectivity matrices were inferred using partial–correlation (PC), cross–correlation (XC), mutual information (MI), and generalized transfer entropy (GTE), as decribed in the Methods section, and finally compared with the ground–truth connectivity.

Fig. 4 shows the Receiver Operating Characteristic (ROC) curves for the respective models for two different fps and low noise (top panels); and for two different noise levels at 50 fps (bottom panels). Each curve represents the average over 10 different network realizations of the simulation with identical number of neurons and average connectivity. The shaded area corresponds to the error given by their respective standard deviation.

Considering the sensitivity to frame rate (Fig. 4, top), the best reconstructions were obtained through GTE, although the quality of reconstruction slightly decreased as the frame rate increased. This is possibly due to our choice of $k = l = 2$, which expects interactions to occur in neighboring time bins, a condition that is fulfilled at 20 fps but that is less satisfied at 50 fps or larger. The results for XC were worse, although the results improved as the frame rate increased, possibly because the timing of the interactions was better resolved. Intermediate results were obtained with the MI and PC reconstructions.

This analysis shows that PC reconstruction achieved better results than XC. Indeed, unlike bivariate methods such as XC, PC is a multivariate method that provides simultaneous analysis of interdependences between three or more processes. Hence, in this sense, XC–reconstruction was unable to distinguish direct and indirect connections falling

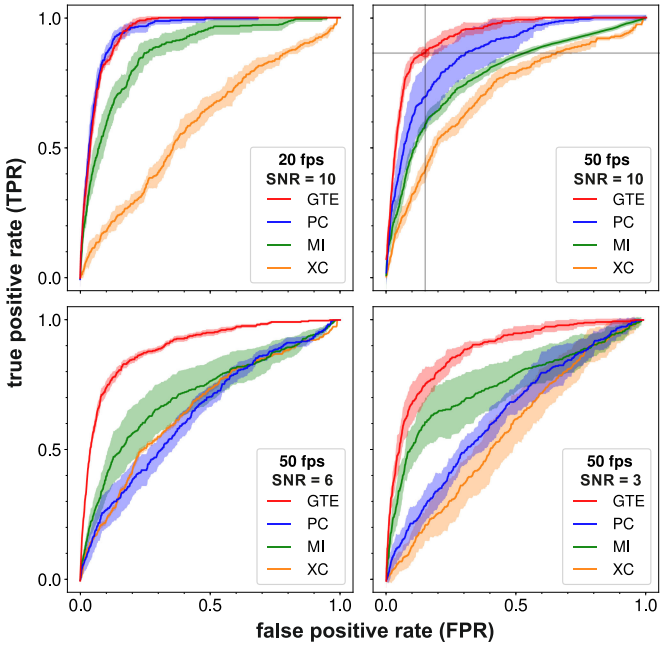


Fig. 4. *Performance of reconstruction strategies on simulations.* Comparison of ROC curves for chosen similarity measures, and for 4 measurement conditions. (Top) Frame rates of 20 and 50 fps, with fixed noise $SNR \simeq 10$. (Bottom) Two noise levels at fixed frame rate (50 fps). The red dot in the top–right panel illustrates the cut–off threshold (15 percent FPR) chosen to quantify the goodness of the reconstruction. The bottom–left panel is the closest to our experimental conditions. All curves are averages using a set of 10 different ground truth topologies in the homogeneous configuration.

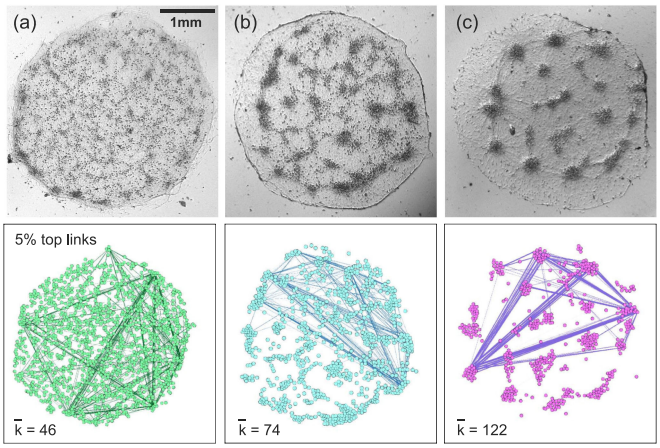


Fig. 5. *GTE effective connectivity of [E+I]–networks* in vitro. (Top) Bright–field images of neuronal cultures ($N \simeq 1,800$ neurons per culture) with aggregation increasing from left to right. (Bottom) Corresponding reconstructed networks, showing the top 5 percent of GTE–ranked links. $\bar{k}$ is the average total connectivity per neuron. (a) Homogeneous ($\mathrm{D}IV$ 14, $\lambda = 0.43$); (b) semi aggregated ($\mathrm{D}IV$ 15, $\lambda = 0.69$); (c) aggregated network ($\mathrm{D}IV$ 14, $\lambda = 0.77$). The thickness of links is proportional to their weight. The directionality of links is omitted for clarity.

short in reconstructing the network's topology. In contrast, an overall good reconstruction was achieved by MI and GTE techniques because they are sensitive to both linear interactions and nonlinear correlations between any pair of neurons. This is also reflected in the analysis of the sensitivity to SNR (Fig. 4, bottom panels), in which both GTE and MI exhibited robustness even when firings were difficult to distinguish from noise. Obviously, for the extreme case in which firings were totally masked by noise, all methods failed at procuring reliable connectivity measures.

We note that the bottom–left panel of Fig. 4 reflects our experimental conditions in terms of fps and SNR. Thus, and taking into account the above results, we chose GTE to infer the effective connectivity in our neuronal cultures.

## 4 Experimental Results: Network Analysis

Fig. 5 provides examples of GTE–inferred effective connectivity in representative homogeneous, semi aggregated and aggregated cultures. Data in all cases was obtained from recordings in which both excitation and inhibition were active ([E+I]–networks). For clarity, only 5 percent of the inferred top–ranked links are represented. Overall, homogeneous networks exhibited a structure in which any neuron could connect to any other, with a rather homogeneous density of connections that extended across the entire culture. Semi aggregated and aggregated cultures also exhibited a long range connectivity, but the density of connections was higher in neuronal aggregates, revealing a relation between connectivity and neuronal proximity. The average total connectivity per neuron in the network, $\bar{k} = \langle k^{\mathrm{in}} + k^{\mathrm{out}} \rangle_N$, gradually increased with aggregation, clearly indicating that, on average, neuronal spatial proximity indeed suffices to substantially enrich the effective connectivity map of neuronal cultures.

Fine details of networks' connectivity are provided in Fig. 6, where we compare the distributions of clustering coefficients CC, in–degree $k^{\mathrm{in}}$ and out–degree $k^{\mathrm{out}}$ for the same homogeneous, semi aggregated, and aggregated cultures of Fig. 5. As a reference, the average CC values for equivalent ER graphs, $\mathrm{CC}^r$, are also shown. A representation of the networks is provided to highlight the location of neurons with the highest total degree $k = k^{\mathrm{in}} + k^{\mathrm{out}}$. High $k$ neurons were uniformly spread across the network for the homogeneous case, and concentrated in dense areas for the other cases. As in the simulations, the distributions were broader, more asymmetric, and with higher average values as aggregation increased, reflecting the role of aggregation in shaping strong connectivity fluctuations. This was particularly clear for the CC distribution of Fig. 6c, which showed peaks at high values. A comparison between Figs. 5c and 6c reveals that these peaks correspond to neurons that form triangles both within their island and between other islands, a feature that strengthens the cohesiveness of the network.

In the following, we analyze the relation between the effective connectivity and the characteristics of the cultures, including average connectivity, small–world features, assortativity and the amount of inhibition, for the development and CNQX–disintegration experiments.

### 4.1 Development Experiments

We explored the maturation of the neuronal cultures without any pharmacological action on the connectivity, i.e., neurons evolved with both excitation and inhibition active ([E+I]–networks). In agreement with a variety of studies [7], [8], [27], [28], the initial ensemble of independent neurons developed rapidly both in connectivity and activity, displaying rich spontaneous activations by DIV 5 [7].

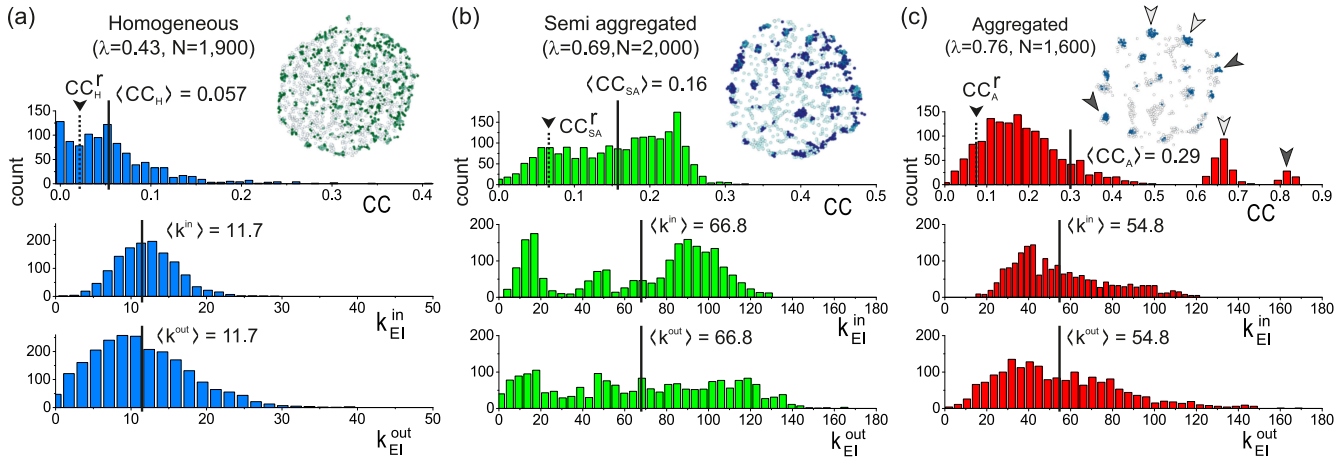


Fig. 6. *Network characterization of GTE–inferred effective connectivity in experiments*. The plots show the distribution of CC, $k^{\text{in}}$ and $k^{\text{out}}$ values for the same individual cultures as Fig. 5, recorded in [E+I] conditions at DIV 15. Solid lines mark the average values of the distributions. Dashed lines with arrow heads indicate the corresponding average CC values for an equivalent ER random graphs, with $\text{CC}^r_H = 0.012$, $\text{CC}^r_{SA} = 0.067$, $\text{CC}^r_A = 0.069$. The networks at the top show the location of neurons, with those exhibiting the highest $\bar{k}$ marked with a darker color. Arrows in the network of panel (c) indicate the location of the neurons with the highest CCs. $N$ indicates the number of neurons in each culture.

All spatial configurations exhibited spontaneous activity characterized by episodes of high coherence (*network bursts*) combined with quiescent intervals. However, aggregated cultures ($\lambda$ high) tended to exhibit spontaneous activity earlier, possibly favored by the aggregation itself that enhanced the swift interconnectivity of groups of neurons.

Fig. 7a shows the frequency of coherent network activity for the three spatial configurations during maturation. Collective activity appeared by DIV 5 and increased quickly for the three configurations, finally reaching a similar firing rate of about 3 burst/min by the second week of development. The growth of activity at early stages was remarkably faster for semi aggregated and aggregated networks, indicating a subtle interplay between activity and connectivity.

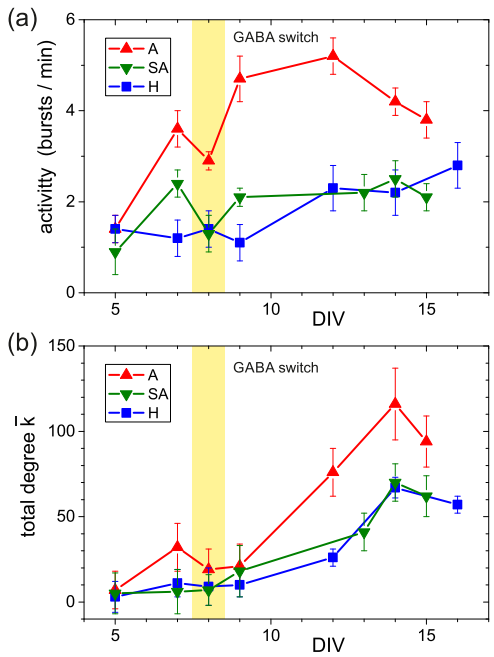


Fig. 7. *Average activity and connectivity during development*. (a) Frequency of network bursts as a function of developmental days *in vitro* (DIV). (b) Total average degree per neuron $\bar{k}$ as a function of DIV. All measurements correspond to [E+I]–networks. Data points are averages over 2 to 6 experiments. Yellow boxes depict the timing of GABA switch.

The corresponding developmental behavior in terms of effective connectivity is provided in Fig. 7b. In general, the total average degree per neuron $\bar{k}$ increased as the cultures matured, with aggregated networks showing a faster development of connections. In all configurations, connectivity stabilized by DIV 8 and later ramped up. This transient feature of stable connectivity can be ascribed to the *GABA switch*, the moment at which inhibitory connections switch from an initially excitatory action to the final inhibitory role. As described later, the GABA switch may temporarily mask the formation of connections, but allows a quantification of the amount of inhibition in the network. Effective connectivity substantially increased after the GABA switch, especially in the aggregated networks. In just 2 weeks, the connectivity of the networks increased by a factor 10, with a total average degree for the different configurations at DIV 15 of $\bar{k} \simeq 56$ (H), 66 (SA) and 96 (A).

The connectivity data for the different network configurations was compared with ER–graphs to assert the existence of small–world (SW) features. To simplify the analysis we treated our networks as undirected and unweighted graphs, so that the average connectivity is given by $\langle k \rangle = (1/N)\sum_i k_i$. For a network to be SW, it has to be highly clustered (much more than a ER–graph) and exhibit small characteristic shortest path lengths (similar to an ER–graph) [29], i.e., it has to fulfill $\kappa = \text{CC}/\text{CC}_R \ll 1$ and $\xi = L/L_R \simeq 1$. Here $\text{CC}_R$ and $L_R$ indicate the values for ER random graphs, which are given by $\text{CC}_R = \langle k \rangle_R / N$ and $L_R = 1/2 + [\ln(N) - \varepsilon]/\langle k \rangle$ [30], respectively, where $\varepsilon \simeq 0.5772$ is the Euler constant.

Comparing the analyzed networks with the ER–graphs, we observed that the ratio of clustering coefficients was $\kappa \simeq 0$ for H and SA networks, and $\kappa \simeq 0.2$ for A networks, values that remain approximately constant during development. On the other hand, the characteristic path length ratio was $\xi \simeq 0.3$ for the three network types, lower than 1. Thus, none of the networks satisfied the criteria for small–worldness, with only a weak tendency to SW for the aggregated one.

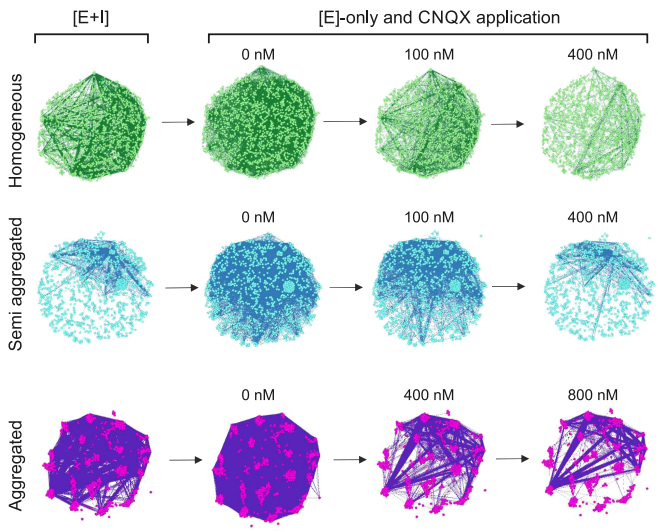


Fig. 8. *GTE effective networks in CNQX disintegration experiments.* The graphs show a representative sequence of effective maps for each of the three spatial configurations. (Top) Homogeneous culture at DIV 15 with $\lambda = 0.43$. (Center) Semi aggregated culture at DIV 14 with $\lambda = 0.58$. (Bottom) Aggregated culture at DIV 14 with $\lambda = 0.77$. CNQX concentrations are indicated above the maps. Only 10 percent of top–ranked links are shown. The directionality of the links is omitted for clarity.

### 4.2 CNQX–Disintegration Experiments

Progressive application of CNQX in a neuronal culture gradually weakens the AMPA–excitatory connections up to the total blockade of neuronal communication, altering the dynamics of the network and, subsequently, its effective connectivity. Connectivity weakening is quantified by the *disintegration coefficient* $\gamma = 1 + [\mathrm{CNQX}]/K_D$, with $K_D = 300$ nM. In our analysis, effective connectivity was first inferred in the [E+I] network data, and then in the [E]–only one for gradually higher CNQX concentrations. In accordance with previous studies [7], we observed that the frequency of spontaneous activity gradually decreased as disintegration progressed until it ceased. The coherence of neuronal activations during disintegration was generally maintained across cultures with different $\lambda$, i.e., all of them showed network bursts.

The evolution of the GTE–inferred effective connectivity upon application of CNQX for different DIV is reported in Table 3 of the SM, which shows only $k^{\mathrm{in}}$ results for clarity, and is graphically illustrated in Fig. 8. The effective connectivity maps show that disintegration is inhomogeneous across the culture, with some neurons retaining a higher number of connections, a feature that markedly increases with aggregation (see also SM, Table 5, available online). In young cultures below DIV 7, i.e., before the GABA switch, the initial blockade of inhibition led to a decrease in $k^{\mathrm{in}}$ since a fraction of the excitatory network was effectually shut down. In more mature cultures with functioning inhibition $k^{\mathrm{in}}$ increased since, on average, the silencing of inhibition jumped up excitation. Subsequent application of CNQX gradually affected the ability of excitatory connections to operate, which were progressively silenced from weaker to stronger. Since activity remained highly coherent along most of the CNQX steps, the effective connectivity exposed the strongest connections and the flow of activity propagation.

Examples of the changes in activity for H and A networks upon CNQX action, for three representative developmental stages, are provided in Fig. 9a. There are three aspects to be

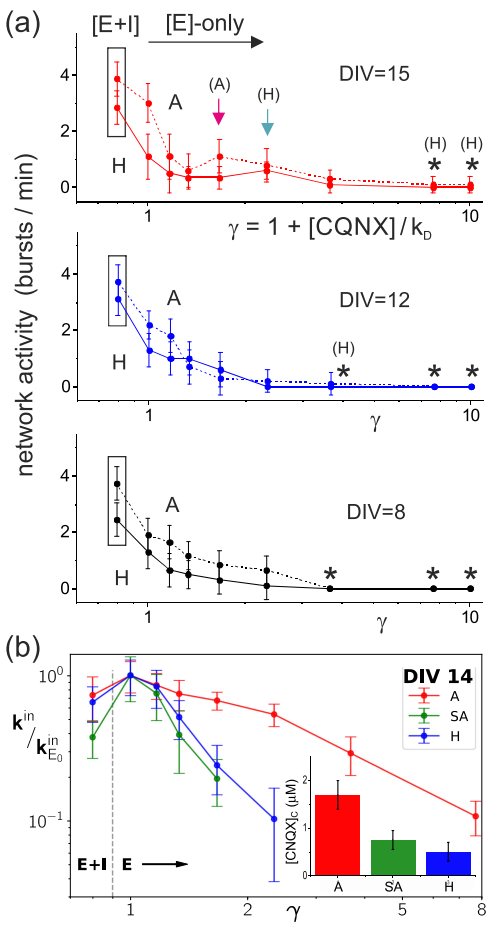


Fig. 9. *Activity and effective connectivity during CNQX disintegration.* (a) Evolution of the average bursting rate as a function of the disintegration coefficient $\gamma$ for three different DIV. Arrows indicate CNQX steps in which activity increased, and asterisks those measurements with no observed activity. The label '(H)' over the asterisk indicates that only homogeneous cultures were silent. (b) Values of normalized in–degree as a function of $\gamma$. $k^{\mathrm{in}}_{E_0}$ corresponds to the $k^{\mathrm{in}}$ value for [E] networks at $[CNQX] = 0$. The data are obtained by averaging over the DIV 13 and 15 values provided in Table 3 of the SM. Inset: critical concentration $[\mathrm{CNQX}]_C$ that halts activity in [E] networks. Each bar is an average over 3 measurements, and corresponds to data at DIV 15 in which groups of 4 cultures with varying $\lambda$ were recorded simultaneously.

noticed. The first one is that the younger the culture, the lower the required concentration of CNQX to silence the network, further corroborating the observation that the number of connections and their strength increase during development. The second one is that aggregated networks are more resilient to CNQX, remaining active at concentrations at which homogeneous networks have already become silent. And the third one is that in mature stages (DIV 15) both networks show sporadic episodes of increased activity upon degradation, which hints at the activation of response mechanisms to stop degradation.

The corresponding evolution of the normalized in–degree $k^{\mathrm{in}}$, shown in Fig. 9b, manifests the overall trend that aggregation favors higher connectivity, and that highly aggregated cultures were able to retain more connections as disintegration progressed. For instance, for $\gamma \simeq 2.33$, A and H cultures retained 60 and 10 percent of the effective input connections, respectively. We must note that connectivity data was inferred from activity, and that a minimum

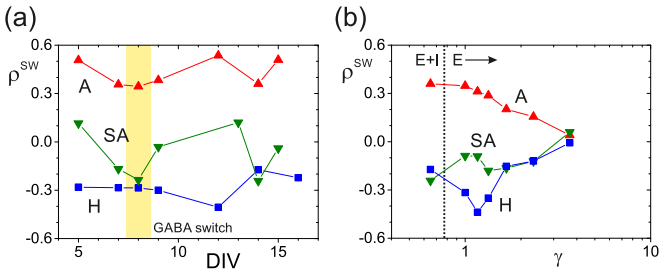


Fig. 10. *Analysis of degree correlations through the Spearman rank correlation* $\rho^{SW}$. (a) Time evolution for [E+I] networks in cultures of each configuration. The yellow box depicts the timing of GABA switch occurrence. (b) Evolution of $\rho^{SW}$ upon CNQX aplication at DIV 14 with the disintegration coefficient $\gamma$. Initial [E+I] values are shown for comparison. Data points are averages over 3 experiments.

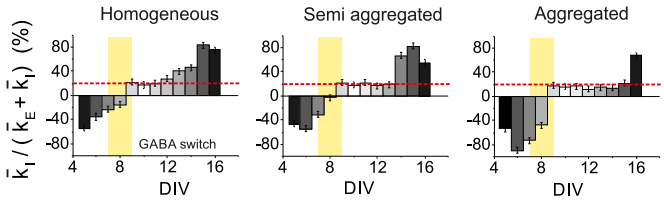


Fig. 11. *Percentage of inhibitory connections during development.* The plots show the time evolution of inhibitory connections during the development of cultures in the three spatial configurations. Inhibitory connections are described by a model of 'subtractive inhibition'. The horizontal dashed red lines are a reference to indicate 20 percent inhibition in cortical cultures. Data are average and standard deviation over 3 experiments at each DIV. Yellow boxes depict the timing of GABA switch occurrence.

activity (about 5 bursts along the recording) was required to build the effective networks. The data shown in Fig. 9b fulfills this condition. However, cultures could exhibit firing events —either in the form of whole–network activations or scattered firings— for higher CNQX concentrations. Indeed, we measured the critical value $[\mathrm{CNQX}]_C$ at which activity ceased at DIV 15 in the different spatial configurations. As shown in the inset of Fig. 9b, the capability of the network to maintain activity increased with the degree of aggregation.

### 4.3 Assortativity

Following Ref. [26], we evaluated the tendency of the inferred effective networks to show assortative or dissassortative traits using the Pearson coefficient ($\rho^{PW}$) and the Spearman rank correlation ($\rho^{SW}$). Both measure the in–out degree correlations, and take into account the weights of the links in the computation. We chose the in–out weighted degree correlations since they reflect the flow of information in the networks. As the results for $\rho^{PW}$ and $\rho^{SW}$ were consistent within error, only the latter is shown here. The evolution of $\rho^{SW}$ with DIV is provided in Fig. 10a, and of $\rho^{SW}$ with the disinegration coefficient $\gamma$ in Fig. 10b.

From DIV 4 to 16, aggregated networks displayed positive values of assortativity ($\overline{\rho}^{SW} \simeq 0.5$), indicating that in–strength neurons attached to others with similar out–strength. In semi aggregated networks the degree distributions were uncorrelated, i.e., with $\overline{\rho}^{SW} \simeq 0$, a structure that is known as neutral assortativity. For comparison, neutral assortativity is characteristic of ER–graphs. Finally, the homogeneous neuronal cultures showed disassortative mixing ($\overline{\rho}^{SW} \simeq -0.28$), indicating that high in–strength nodes tended to attach to low out–strength nodes.

For the CNQX–disintegration experiments, at DIV 14 homogeneous cultures before disintegration were dissassortative ($\rho^{SW} \simeq -0.25$), the semi aggregated ones were neutral ($\simeq -0.04$), and the aggregated ones were assortative ($\simeq 0.36$). These values gradually changed as disintegration took action and, as shown in Fig. 10b, there was a tendency of all networks to become neutral. For the aggregated configuration, we hypothesize that aggregates behave as an assembly of interconnected islands, which break off at the end when activity ceases. For the homogeneous and semi aggregated networks, disintegration brings to light the nodes with the highest number of connections, and the networks become more assortative until activity is lost.

### 4.4 Inhibition

The amount of inhibition in the inferred effective connectivity networks was calculated using the approach of 'subtractive inhibition' [31], [32]. In this approach, the average inhibitory connectivity is given by $\overline{k}_I = \overline{k}_E - \overline{k}_{EI}$, where $\overline{k}_E$ and $\overline{k}_{EI}$ are, respectively, the average connectivity values inferred from [E]–only and [E+I] measurements on the same culture. This relation assumes that excitatory and inhibitory synapses have similar strengths and that the average EPSC and IPSC amplitudes are practically equivalent. In other words, this model assumes that the effect of inhibitory connections is to reduce the excitatory ones by the same amount.

The comparison of the data for [E+I] and [E] networks allowed us to follow the emergence of inhibition during development, as well as to estimate the fraction of inhibition. Fig. 11 shows the percentage of inhibitory connections along DIV for the H, SA and A spatial arrangements. Inhibition emerged in all cases by DIV 9, when the GABA–switch occurred, reaching then a percentage that remained around 20 percent for the next 5 days. Very high values were obtained above DIV 14, when the cultures were more mature. Comparison with simulations suggests that the linear approximation assumed above is not valid in this regime and that a more complex nonlinear model should be considered.

## 5 Discussion

### 5.1 Activity and Effective Connectivity

Effective connectivity arises from a complex interplay between the architecture of the network and the dynamics of the neurons. It may therefore reflect the flow of information and the spatio–temporal structure of activity propagation. In mouse slice preparations, for instance, it was shown that 70 percent of the information passed through only 20 percent of the neurons in the network [15]. Hence, effective connectivity may not necessarily coincide with the structural blueprint of the network. This difficulty reflects an important debate in the neuroscience community, since accessing structural information from dynamics, i.e., non–invasively, is pivotal for the study of the brain and its malfunction due to disease.

In this direction numerical simulations are very useful at providing a framework to model neuronal networks and to investigate under which conditions the effective connectivity is a good proxy of the structural one. Stetter et al. [4]

used numerical simulations to show that both the connectivity inference algorithm and the dynamic state of the network—e.g., network bursts or monosynaptic interactions—must be chosen appropriately. Following his work, and based on our simulations, we chose GTE as the algorithm to infer the effective connectivity. Of importance in GTE is the treatment of the fluorescence data by *conditioning*, which eliminates the repeated activations upon neuronal bursting. This treatment provides a better balance between coherent activations and monosynaptic, neuron–to–neuron interactions.

Despite conditioning, we must note that coherent activations in neuronal cultures dominate the dynamic repertoire, and that activity outside these episodes is scarce. Hence, given the short duration of our recordings, it may occur that the inferred effective connectivity reflects in great measure the neuronal correlations during the propagation of the bursting episodes. In the context of the *noise focusing* phenomena [8] it was shown that coherent activity preferentially initiates in specific areas of a neuronal culture termed *focusing points* and that they emerge from a complex trade–off between connectivity and noise–amplified activity. An analysis of the foci of activity in our cultures revealed that they concord with the regions of high *effective* connectivity. We also observed that high values of $k^{\text{out}} - k^{\text{in}}$ often coincided with high neuronal densities $\rho$ (see SM, Fig. S4, available online), indicating that neuronal aggregation favored the initiation of activity, a trait also observed in other studies [33]. The weakening of synapses by CNQX affects these foci of activity and the flow of information, which is reflected by changes in the effective connectivity maps.

Ito et al. [12] argued in the analysis of effective connectivity in organotypic cultures that monosynaptic interactions are the ones that better portray the anatomical connectivity. Their assertion agrees with our simulations and other studies [4], [34]. Thus, for the inferred effective connectivity to be a good proxy of the structural one, one needs to substantially increment the occurrence of these monosynaptic interactions. We are therefore devising experiments in which these interactions would be favored, either through pharmacological action, a variation of the balance of ions in the recording medium, or external stimulation.

### 5.2 Connectivity Values and Quorum Percolation

The effective connectivity analyses provided an estimation of the connectivity of the networks, with $\bar{k}_E^{\text{in}} \simeq 50$ for H and SA networks, and $\bar{k}_E^{\text{in}} \simeq 120$ for A ones (see Table 3, SM, available online). These values can be contrasted with an alternative approach, namely with the study of the disintegration of the giant component $g$ in quorum percolation [31], [35]. In this approach, the giant component $g$ of a network was defined as the largest fraction of neurons that fired together in response to an electrical stimulation, and its size was investigated as the excitatory network connectivity was reduced with CNQX. The giant component is constituted by those neurons that retain sufficient input connections at each CNQX step. The required number of inputs for a neuron to remain in the giant component was expressed as $m = m_0\gamma$. Here $m_0 \simeq 15$ represents the minimum number of connections a neuron requires to fire. In the absence of inhibition, the critical value of $m$, termed $m_E$, at which $g \simeq 0$ is related to the average input connectivity of the network, $\bar{k}_E^{\text{in}} \simeq m_E$ [31], [32], [35]. For homogeneous cultures with a density similar to ours $\bar{k}_E^{\text{in}} \simeq 30$ was obtained, which is consistent with our results.

Let us emphasize that the giant component analysis provides information on the average *structural* connectivity, while in our study we determined the *effective* connectivity at single neuron level. We remark again that is it difficult to quantify how well the effective connectivity derived from activity mirrors the structural one. One would need to determine the *experimental ground truth topology*, which would require approaches such as electrophysiological measurements or staining of axons.

### 5.3 Aggregation and Connectivity

Although the nominal density upon plating was the same in all cultures, aggregation caused strong variability at a local scale. The size of the aggregates was about $0.25$ mm$^2$ and they typically contained $100$ neurons. While the density was $\rho_{\text{H}} \simeq 250$ neurons/mm$^2$ in homogeneous cultures, in aggregated cultures it was $\rho_{\text{A}} \simeq 500$ inside the aggregates and $\rho_{\text{O}} \simeq 100$ neurons/mm$^2$ outside them. This difference is remarkable. In the setting of quorum percolation outlined above, Soriano et al. estimated that the number of excitatory input connections increases with the density [31], from $\bar{k}_E^{\text{in}} \simeq 30$ for $\rho \simeq 100$ to $\bar{k}_E^{\text{in}} \simeq 80$ for $\rho \simeq 500$ neurons/mm$^2$. Hence, one may expect a factor 3 more structural connections within aggregates than between aggregates or isolated neurons.

A substantial increase in connectivity in dense areas of a neuronal culture was also observed by Maccione et al. [11] in MEAs. They used cross–correlation analysis combined with spatio–temporal filtering and staining of connections to determine the strongest effective links of the network, and observed that neuronal aggregates contained about 55 percent more links than their sparser neighborhood. On the other hand, a recent study by Lonardoni et al. [36] showed that distance–based connectivity formation during the development of neuronal circuits sufficed to create nuclei of strong interconnectivity, which were central in initiating coherent network dynamics. This result suggests that aggregation promotes both activity and connectivity, and agrees with our observation that aggregated and semi aggregated cultures exhibit a fast growth of these quantities during early development (Fig. 7).

The increase of structural connectivity upon aggregation highlights that metric correlations may prove essential to understand the behavior of neuronal networks. Hernández-Navarro et al. [19] recently showed that the role of spatial embedding in the structure and dynamics of networks can be quantified in terms of the degree of aggregation $\lambda$ and the relative axonal length $\delta = a/L$, where $a$ is the average axonal length and $L$ the diameter of the culture.

Within this framework we consider the following cases. The situation of $\lambda \to 0$ and $\delta \to \infty$ corresponds to a perfectly homogeneous network with long–range neuronal interconnectivity, leading to a *mean field* scenario in which spatial embedding is irrelevant. Our homogeneous cultures approach this condition, with effective connections homogeneously distributed and extending over the entire culture.

The evolution from $\delta \to 0$ to $\delta \to \infty$ corresponds to a transition from a local connectivity to a mean field one, and would be the equivalent of our development experiments. However, a direct comparison is not possible since the same culture could not be measured at different DIV. Additionally, our cultures are relatively small, and therefore it may occur that the first observation of coherent activity ($\mathrm{D}IV \simeq 5$) corresponds to a situation of already large $\delta$.

Finally, the situation of $\lambda \simeq 0.8$ and $0.1 \lesssim \delta \lesssim 1$, which balances local and long–range connectivity, corresponds to our aggregated configuration. The analysis of the cultures through the effective connectivity reflects this physical richness. Viewing the network as a whole, the average connectivity $\bar{k}$ consistently increased with aggregation; and at a local scale aggregation favored strong binding within islands of neurons that was combined with long–range interconnectivity.

We emphasize that a balance between short- and long-range connections is crucial to observe network wide coherent activations. This is the case for all cultures explored in this work regardless of their aggregation. However, we observed, in the CNQX–disintegration experiments, that for large $\lambda$ this balance facilitated activity to fragment into sub–networks that maintained some sort of population activity. These observations could not be analyzed in detail since network activity for large [CNQX] was not sufficiently rich for reliable connectivity inference. The extreme case of highly aggregated networks corresponds to cultures constituted by interconnected *neurospheres* [26], [37], a configuration that displays modular dynamics, with groups of aggregates firing together in small communities rather than in a coherent manner.

### 5.4 Assortativity

The fact that the assortativity traits are markedly distinct for different aggregation levels indicate that neuronal proximity fosters degree–degree correlations that persist along development. Moreover, one has to take into account that our extracted degree–degree correlations are effective, i.e., extracted from dynamics, and that assortativity in this *effective* perspective may also reflect the tendency of highly co–active neurons to strengthen their connectivity.

Our results show that aggregated cultures are assortative ($\overline{\rho}^{SW} \simeq 0.50$), semi aggregated are neutral, and homogeneous are disassortative ($\overline{\rho}^{SW} \simeq -0.28$). Our numerical simulations show that aggregated networks are also assortative, with $\overline{\rho}^{SW} \simeq 0.32$, while homogeneous are neutral. Other studies in neuronal cultures also reported strong assortative mixing in aggregated networks [26], and neutral [26] or dissassortative mixing [10] in homogeneous networks. Given the discrepancy on homogeneous cultures, further experiments and analyses are needed to understand its origin.

### 5.5 Inhibition

The use of the 'subtraction' rule $k_I \simeq k_E - k_{EI}$ sufficed to estimate the amount of inhibition in the network and to time the occurrence of the GABA switch. However, this rule is based on the quorum percolation model, which assumes that an inhibitory connection just cancels out an equivalent excitatory one [31], [32]. In reality, the excitatory and inhibitory sub–networks have a complex interrelation that requires accurate modeling. Orlandi et al. [34] investigated *in silico* the ability to resolve the excitatory and inhibitory sub–networks, using GTE and combining the data of [E+I] and [E]-only effective networks inferred from spontaneous activity. They concluded that spontaneous activity did not convey sufficient information to uncover both networks, and that only with stimulation reliable information could be extracted.

## 6 Conclusion

Our study showed that metric correlations inherited from spatial aggregation fostered the interconnectivity among neighboring neurons. Spontaneous activity along different degrees of aggregation and experimental conditions was examined to infer the effective connectivity of the networks. We observed that the average connectivity of the cultures rapidly increased during development, and with average excitatory connectivities of $\bar{k}_E^{\mathrm{in}} \simeq 50$ for homogeneous and semi aggregated networks and $\bar{k}_E^{\mathrm{in}} \simeq 120$ for aggregated ones, and with 20 percent inhibitory connections. The former networks exhibited dissassortative or neutral degree–degree correlations, while the latter were assortative. Aggregated networks also exhibited stronger resilience to the loss of connections through chemical action. Overall, our study underlines the importance of neuronal spatial arrangement and metric correlation in shaping connectivity and activity traits in living neuronal networks.

## 7 Methods

### 7.1 Neuronal Cultures and Experimental Procedure

Here we describe the preparation of the neuronal cultures, their monitoring through calcium fluorescence imaging, and the modification of neuronal connectivity through pharmacological action.

#### 7.1.1 *Neuronal Cultures*

We used rat cortical neurons from 19–day–old Sprague–Dawley embryos. All the procedures were approved by the Ethical Committee for Animal Experimentation of the University of Barcelona, under order DMAH-5461.

Neuronal cultures were prepared as follows. Cortices were isolated from embryonic brains and dissociated through gentle pipetting. The resulting ensemble of neurons and glia were plated on 13 mm diameter glass coverslips (#1 Marienfeld–Superior) that incorporated a perforated polydimethylsiloxane (PDMS) mask (Fig. 1a). The mask was 1 mm thick and contained a set of 4 circular holes 3 mm in diameter. The combined PDMS–glass structure effectively provided 4 *mini cultures* that could be simultaneously monitored with the optical system.

Prior plating, glasses were cleaned with nitric acid and double–distilled water (DDW), flamed in ethanol and autoclaved in the presence of the PDMS mask, ensuring a firm bond between the two materials. Mini cultures with contrasting neuronal spatial arrangements were prepared by coating the glasses with preset concentrations of the adhesive protein Poly–L–Lysine (PLL, Sigma). The higher the concentration of PLL, the higher the homogeneity of the

network (Fig. 1b). Standard *Homogeneous* (H) cultures were prepared by treating the glasses overnight with $10$ $\mu$g/ml PLL in Borate Buffer. We note that some degree of aggregation was always observed despite the strong anchoring of the neurons. A factor $10$ dilution of this base concentration provided *semi aggregated* (SA) cultures, while a factor $100$ dilution (or directly total absence of PLL) provided *aggregated* (A) cultures.

Neurons were seeded onto the combined glass–PDMS structure in the presence of *plating medium* for the development of both neurons and glia. Cultures were incubated at 37 °C, 95 percent humidity, and 5 percent $CO_2$. At *day in vitro* 4 the medium was switched to *changing medium* for 3 days to limit glia growth, and thereafter to *final medium*. This medium was refreshed every 3 days by replacing half of the culture well volume. Full details of materials preparation and culture media are provided in Refs. [7], [8].

Neurons were plated with a nominal density of $5{,}000$ neurons/mm$^2$, providing a final density (measured over the recorded images) around $300$ neurons/mm$^2$, i.e., about $2{,}000$ neurons per mini culture.

#### 7.1.2 Calcium Fluorescence Imaging and Data Acquisition

Prior to imaging, the PDMS mask was removed to ensure total independence of the 4 mini cultures, which were then incubated for $40$ min in External Medium (EM, consisting of 128 mM NaCl, 1 mM $CaCl_2$, 1 mM $MgCl_2$, 45 mM sucrose, 10 mM glucose, and 0.01 Hepes, adjusted to pH 7.4), in the presence of the calcium sensitive dye Fluo–4-AM (Life), with 4 $\mu$g Fluo–4 per ml of EM. The culture was washed with fresh EM after incubation, placed in a bottom–glass petri dish filled with 4 ml of EM, and attached to a thermal bath platform at 25 °C. The platform was finally mounted on a Zeiss Axiovert C25 inverted microscope equipped for fluorescence imaging.

Spontaneous neuronal activity was monitored through a Hamamatsu Orca Flash 2.8 camera. Neurons appeared as bright objects upon firing. Activity was recorded at 45 frames per second, with a frame size of $960 \times 720$ pixels and a field of view of $8.2 \times 6.1$ mm$^2$ that contained 4 mini cultures. Activity was recorded for $10 - 30$ min.

At the end of the recording neurons were manually identified as Regions of Interest (ROIs) over the images, with typically about $2{,}000$ ROIs per mini culture. The recorded data was then processed to extract for each identified neuron its fluorescence trace $f(t)$, which was finally expressed as $\%\text{DFF} \equiv 100 * (f - f_0)/f_0$, with $f_0$ the average brightness of the neuron at rest.

#### 7.1.3 Degree of Aggregation $\lambda$

It is computed through the normalized area under the 'Lorenz curve' (Fig. 1c) as follows. The identified neurons were laid out on a surface that contained a grid of $100 \times 100$ $\mu$m. The number of neurons in each grid element was then counted. The Lorenz curve was then constructed by plotting the cumulated number of neurons as a function of the cumulated area fraction $a$, and normalizing both axes between $0$ and $1$. By denoting $S$ as the area comprised between the Lorenz curve and the bisector, $\lambda$ was then set as $\lambda = 2S$.

In our cultures $\lambda$ typically varied between $0.3$ and $0.85$. Its value procured the classification of cultures stated above as homogeneous ($\lambda \leq 0.5$), semi aggregated ($0.5 < \lambda \leq 0.7$), and aggregated ($\lambda > 0.7$).

#### 7.1.4 Pharmacology and Experimental Protocols

Rat cortical neuronal cultures contain 80 percent excitatory neurons and 20 percent inhibitory ones [31]. Excitatory connections are mediated through AMPA–glutamate and NMDA receptors. while inhibitory ones are mostly mediated through $GABA_A$ receptors. By applying appropriate doses of a receptor's antagonists the connectivity of the network can be varied, and the resulting spontaneous activity explored.

Our study encompassed two groups of experiments, namely *development* and *connectivity weakening*. The total number of monitored cultures was 74 (H: 23, SA: 27, A: 24).

*Development Experiments.* We monitored neuronal activity over the first three weeks of network development. A batch of 24 identical wells was prepared. Starting at DIV 5, a culture was selected and its spontaneous activity recorded for 30 min. Another culture was then selected 24 h later and measured. This procedure was then repeated for 3 weeks. No connectivity blockers of any kind were used in these experiments, i.e., both excitatory and inhibitory connections were active ( [E+I]–network).

*Connectivity Weakening Experiments.* Connectivity disintegration was achieved by gradually blocking the AMPA–glutamate receptors in excitatory neurons through the antagonist CNQX. Experiments were carried out in groups of cultures prepared in 24 wells, but studied at different developmental time points in the range $8 - 16$ DIV. In each experiment, activity was first recorded for 15 min with no blockers of any kind ([E+I]–network). Next, NMDA excitatory receptors and $GABA_A$ inhibitory receptors were completely blocked with 20 $\mu$M APV and 40 $\mu$M bicuculline, their respective antagonists. After 10 min waiting time for the drugs to take effect, spontaneous activity was measured for 15 min in excitatory (AMPA–glutamate only) conditions ([E]–only network). Then, a sequence of gradual application of CNQX was started, with concentrations of $50$, $100$, $200$, $400$, $800$, and $2{,}000$ nM. Each application was followed by a $5$ min waiting time for the drug to act and a spontaneous activity recording of $15$ min. The total duration of the experiment was about 2 h. Results are reported in terms of $\gamma = 1 + [\text{CNQX}]/K_d$, where $K_d = 300$ nM is the dissociation constant of CNQX, i.e., the concentration at which 50 percent of the AMPA receptors are blocked [31]. Conceptually, $m = m_0\gamma$ is the number of inputs that are required onto a neuron for it to fire, with $m_0 \simeq 15$ the minimum number of simultaneous inputs (*quorum*) [31], [32], [35]. We verified that the duration of the experiment did not compromise the health of the culture, by repeating the first measurement after washing off the drug antagonists [7], [31].

### 7.2 Numerical Simulations

We used algorithms to generate sets of neuronal networks of a given spatial structure, and simulated their spontaneous dynamics. First, the best simulation parameters were chosen from 400 simulations, selecting those that

reproduced the experimental behavior (SM, Fig. 3, available online). Second, H, SA, A configurations were explored in additional 100 simulations. Third, the dynamics of 10 networks were calculated to unveil the best effective connectivity inference method.

#### 7.2.1 Construction of Spatial Networks

To mimic the spatial distribution of neuronal cultures, homogeneous and aggregated networks were grown on substrates partitioned into two–color subdomains (Figs. 2a and 2b).

*Homogeneous Networks (Fig. 2c).* A set of $N$ neurons was randomly placed on a circular area 3 mm in diameter. Each neuron was modeled as a circular cell body (soma) with fixed diameter $\phi_s = 15$ $\mu$m. Occupation density was set in the range $\rho \simeq [100 - 350]$ neurons/mm$^2$. Neurons were labeled as either excitatory with probability $p_E = 0.8$ or inhibitory with $p_I = 0.2$.

The growth processes of axons and dendrites were generated using the spatial metric construction described in [8]. Briefly, axonal growth was simulated as a random process with final axonal length given by a Rayleigh distribution. Dendritic trees were modeled as disks whose diameter $\phi_d$ was drawn from a Gaussian distribution. When the axon of a neuron $i$ intersected the dendrite tree of a neuron $j$ connection $i \to j$ was recorded with probability $\alpha$. For each set of networks a values of $\alpha$ was chosen in the range of $[0.3 - 1]$. The parameters used for the generation of the networks are provided in Ref. [8].

*Aggregated Networks (Fig. 2d).* They were created by dividing the $N$ neurons into two subsets. The first one was distributed homogeneously over the 3 mm diameter substrate with a total number of neurons $N_H$; the second one comprised $N_A$ neurons that were split into 15 islands of approximately 0.2 mm in diameter and randomly distributed over the substrate. Connectivity within each subset was then established following the above rules. The subsets were then merged by eliminating those neurons of the homogeneous subset that fell within an island and their connections were assigned to the closest neurons in the island. This construction ensured that both subsets were interconnected within and between them. Different neuronal densities were explored in the simulations but maintaining the ratio $N_A/N \simeq 0.2$. The creation of an aggregated network through this overlap procedure is sketched in Fig. 2b.

*Boundary conditions* were set as follows. The edge of the circular substrate was treated as a *reflective wall* where the reflected axonal section had the same angle to the normal of the wall in the direction opposite to the incident section.

#### 7.2.2 Dynamic Model

The soma dynamics and the generation of action potentials was described using a quadratic integrate–and–fire model with adaptation [38], [39], [40]. In the reduced form its equations are

$$\tau_c \dot{v} = k(v - v_r)(v - v_t) - u + I + \eta, \tag{1}$$

$$\tau_a \dot{u} = b(v - v_r) - u, \tag{2}$$

$$\text{if} \quad v \geq v_p \quad \text{then} \quad v \leftarrow v_c, u \leftarrow u + d. \tag{3}$$

Here $v$ is the fast soma membrane potential, $u$ the slow inhibitory current, $\tau_c$ and $\tau_a$ time constants, $I$ the synaptic inputs, and $\eta$ a noise term that reflects the spontaneous emission of spikes. The rest of variables are parameters to set the neuronal firing properties.

These equations adequately describe neuronal activity. Below the threshold potential $v_t$, the inputs are not sufficient to trigger instability and the membrane potential relaxes towards its resting value $v_r$. Above $v_t$, inputs trigger fast increase in potential, up to a preset peak value $v_p$ leading to the generation of a spike, after which $v$ is reset to $v_c$.

Each synapse between two neurons has its own dynamics, which may affect network function. This model assumes that, upon generation of a *spike* or action potential (AP), all presynaptic terminals of that neuron release neurotransmitters simultaneously. Axonal propagation delays are neglected given that the propagation velocity of APs ($\simeq 1$ m/s) is much faster than the velocity of neurotransmitters' release and subsequent stimulation ($\simeq 0.15$ m/s).

The rate of synaptic depression $D$ describes the depletion process of glutamate presynaptic vesicles [41]. Depression is modeled as [38]

$$\frac{d}{dt} D = \frac{1}{\tau_D}(1 - D) - (1 - \beta) D \delta(t - t_m), \tag{4}$$

where $\tau_D$ is the characteristic recovery time of synaptic vesicles [42]. It controls the inter–burst interval and takes values in the range of $0.5 - 20$ s for our cultures. In Eq. (4), $D$ is initially set as 1 (no depression) and decreases by $D \to \beta D$ ($0 < \beta < 1$) after each current injection.

We note that, the depression mechanism leads to an increase in the sensitivity of a neuron to subtle changes in the firing patterns of its afferents [43]. Thus, like other forms of short–term plasticity, synaptic depression causes the response of a neuron to depend on the previous history of afferent firings.

The parameters used in the simulations are provided in Ref. [8]. Using these parameters the neurons exhibit *regular spiking* behavior (RS type) combined with *bursts* (short neuronal spike trains), as shown in Fig. 3. At a network level, neurons display coherent activations or *network bursts*, as in the experiments. The dynamic model is completed with the incorporation of the calcium dynamics and Gaussian noise, so that fluorescence data mimics the experimental one.

To compare simulations with different noise levels we define the signal–to–noise ratio as [6]

$$\text{SNR} = \frac{A_{\text{spike}}}{\text{SD}_{\text{noise}}}, \tag{5}$$

where $A_{\text{spike}}$ is the amplitude of a single spike event and $\text{SD}_{\text{noise}}$ the standard deviation of the noise, with both quantities expressed in %DFF units. In experiments SNR $\simeq 5$, and in simulations it was varied in the range $[3 - 10]$ (Fig. 3).

### 7.3 Connectivity Inference Tools

#### 7.3.1 Neuronal Activity Sequences

The recorded or simulated fluorescence time series were converted into *binary* activity sequences, i.e., trains of either detected activity (1), corresponding to a sharp rise in the

signal, or silent intervals (0), as described in [4]. The binary sequence of a neuron $i$ was computed from its fluorescence signal $F_i(t)$ (in %DFF units) through two transformations. First, the discrete difference operator ($\delta F_{i,n} = F_{i,n+1} - F_{i,n}$) was applied to reduce the probability that random fluorescence oscillations would trigger the detection of a spike. Here $n \in [1, N]$, with $N$ the number of data points in the time series. Second, *conditioning* was applied to the resulting time series. This filter accepts a spike if the average of $\delta F_{i,n}$ over the full population of neurons is below the conditioning level $\tilde{c}$ at time step $i$, chosen so that spikes recorded during high global activity are discarded.

#### 7.3.2 Similarity Measures

The connectivity traits of the network are assessed based on the following similarity measures of the activity of pairs of neurons. *Effective* networks were obtained with inference methods which detect causal relations between nodes and yield directed graphs.

*Cross–correlation* assigns the largest cross–correlogram peak over a range of delay times $\delta$,

$$\mathrm{XC}_{j\to i} = \max_{0\le\delta\le t_{max} c_n < \tilde{c}} \{\rho_{ij}\}, \tag{6}$$

$$\rho_{ij} = \frac{\sum_{n=1}^{T}(x_{in}-\mu_i)(x_{jn}-\mu_j)}{(T-1)\,\sigma_i\,\sigma_j}, \tag{7}$$

where $t_{max} = 200$ ms and $\tilde{c}$ is the conditioning level. The binary signal of activity of neuron $k$ is $\{x_k\}$, its average is $\mu_i$ and standard deviation is $\sigma_i$. The obtained connectivity matrix is weighted and undirected because of the symmetric roles of $i$ and $j$ in the equation.

*Partial correlation* computes the correlation between neurons $i$ and $j$ after removal of the dependence on neuron $k$ [44]. It is a multivariate linear symmetric measure that is calculated using

$$\mathrm{PC}_{j\to i} = \max_{0\le\delta\le t_{max} c_n < \tilde{c}} \left\{\rho_{ij}^{k}\right\}, \tag{8}$$

$$\rho_{ij}^{k} = \frac{\rho_{ij} - \rho_{ik}\,\rho_{jk}}{\sqrt{(1-\rho_{ik}^2)(1-\rho_{jk}^2)}}. \tag{9}$$

*Mutual information* is a nonlinear and symmetric measure of the statistically shared information between two random variables [45], [46]. The delay $\delta$ was chosen to maximize MI scores

$$\mathrm{MI}_{Y\to X} = \max_{\delta\in[0,t_{\max}]} \left\{ -\sum p(x_n, y_{n-\delta}|c_n < \tilde{c}) \times \log \frac{p(x_n, y_{n-\delta}|c_n < \tilde{c})}{p(x_n|c_n < \tilde{c})p(y_{n-\delta}|c_n < \tilde{c})} \right\}, \tag{10}$$

where $p(x_n, y_{n-\delta})$ denotes the joint probability of $X$ and $Y$ at temporal delay $\delta$, and $p(x_n)$ and $p(y_n)$ are the marginal probabilities of X and Y, respectively. The sum goes over all possible values of $x_n$ and $y_{n-\delta}$.

*Transfer Entropy* (TE) measures the amount of information transferred from $Y$ to $X$ [45]. This measure is nonlinear and non–symmetric in $X$ and $Y$. We used the extended *Generalized Transfer Entropy* that accounts for the conditioning of the fluorescence signal through $\tilde{c}$ [4], [47],

$$GTE_{Y\to X} = -\sum p\left(x_{n+1}, x_n^{(k)}, y_n^{(k)}|c_{n+1} < \tilde{c}\right) \times \log_2 \frac{p(x_{n+1}|x_n^{(k)}, y_n^{(l)}, c_{n+1} < \tilde{c})}{p(x_{n+1}|x_n^{(k)}, c_{n+1} < \tilde{c})}. \tag{11}$$

Here $k$ is the Markov order of the model and the length of the vectors $\{x_n^{(k)}\}$. The sum goes over all possible values of $x_{n+1}$, $x_n^{(k)}$, $y_n^{(k)}$, and $y_n^{(l)}$. Since the synaptic time constants ($\simeq 1$ ms) are much smaller than the acquisition times of the recordings ($\simeq 20$ ms), we chose $k \approx 2$ with $l = k$.

### 7.4 Validation of Inference Methods

The similarity measures provide an *adjacency matrix* $A$ whose elements $w_{ij}$ are the connectivity *weights* among firing neurons. Spurious connections were removed using a confidence threshold. Weak and non–significant links were filtered out using surrogates to generate *null models* of the connectivity matrices. The quality of reconstruction was assessed on simulated networks, which allowed us to compare the inferred connectivity matrices and the ground–truth structural matrix.

This analysis allowed us to choose the most appropriate reconstruction method and to select the optimal threshold to define top–ranked links.

#### 7.4.1 Surrogates

Surrogates were generated from the neuron activation signals to preserve the structure of the data while destroying temporal correlations between neurons.

In order to preserve the firing statistics of neurons, the *jitter* method was chosen to generate surrogates. The timing of each spike is perturbed by an amount drawn from a Gaussian distribution of mean zero and standard deviation $\sigma = 20$ ms that matches the upper time delay between neurons [48]. Because the perturbation has zero mean, the inter–spike–interval distribution is preserved along with the modulations in population activity. Moreover, the number of spikes per neuron remains invariant but the (intrinsic) time correlations between neurons are destroyed.

#### 7.4.2 Significant Links

We chose to generate 100 surrogates per experiment to correctly estimate their distribution without an excessive computational cost. By denoting $A^S = \left\langle w_{ij}^S \right\rangle$ the average value of the surrogates' weights and $\sigma_S$ the standard deviation of their distribution, only those scores of the original GTE data fulfilling $w_{ij}^{\mathrm{ORI} > A + 2.33\,\sigma_S}$ were considered significant and retained. This selection provided a confidence level of 98 percent. These final links were the ones used to compute the network measures.

To obtain unweighted graphs the weights are binarized by assigning the weight 1 to all significant links, the remaining weights are set to zero.

### 7.5 Network Measures

For directed networks, the *total degree* $k_i$ is the sum of the numbers of ingoing ($k_i^{\mathrm{in}}$) and outgoing ($k_i^{\mathrm{out}}$) links at node $i$. The *average total degree per neuron* is then given by

$\bar{k} = (1/N)\sum_i (k_i^{\text{in}} + k_i^{\text{out}})$. For weighted networks one also considers the *strength* as $s_i = \sum_j w_{ij}$.

The *characteristic shortest path length* $L$ is the mean of shortest paths $d_{ij}$ for all the possible pairs of network nodes,

$$L = \frac{1}{N(N-1)} \sum_{i \neq j} d_{ij}, \tag{12}$$

$$d_{ij} = \sum_{a_{ij} \in g_{i \to j}} \left( \frac{1}{w_{ij}} \right), \tag{13}$$

with $g_{i \to j}$ the directed shortest weighted path from $i$ to $j$.

The *clustering coefficient* CC measures the cohesiveness of the network at a local scale. It is computed as the ratio between the number of triangles with $i$ as one vertex and the number of all possible triangles that $i$ could form [49]

$$\text{CC} = \left\langle \frac{\left(A + A^T\right)^3_{ii}}{2T_i} \right\rangle_i, \tag{14}$$

where $A^T$ is the transpose of the adjacency matrix $A$, $\langle \rangle_i$ denotes average over index $i$, and $T_i = k_i(k_i - 1) - 2k_i^{\leftrightarrow}$, with $k_i^{\leftrightarrow}$ is the number of bidirectional links at node $i$.

The *degree correlation* quantifies the likelihood that nodes attach to other nodes of similar (*assortative*) or dissimilar (*disassortative*) degree [50]. For weighted and directed networks, it is computed using the 'Pearson Weighted' (PW) or the 'Spearman Weighted' correlation coefficients of the degree as described in Ref. [26]. The estimation of the error in the assortativity value is computed through the bootstrap algorithm [51] considering 1,000 random samples of the data.

## Acknowledgments

The authors would like to thank S. Teller and D. Malagarriga for fruitful discussions. This work was supported by the Spanish Ministerio de Economia y Competitividad through projects FIS2013-41144-P, MAT2013-40590-P, and MAT2015-69-777-REDT; and by the Generalitat de Catalunya through grant 2014-SGR-878. This study is part of MESO-BRAIN. The MESO-BRAIN Project has received funding from the European Union's Horizon 2020 Research and Innovation Programme under Grant Agreement No. 713140.

## References

[1] C. J. Honey, J.-P. Thivierge, and O. Sporns, "Can structure predict function in the human brain?" *NeuroImage*, vol. 52, no. 3, pp. 766–776, 2010.

[2] M. Schröter, O. Paulsen, and E. T. Bullmore, "Micro-connectomics: Probing the organization of neuronal networks at the cellular scale," *Nature Rev. Neurosci.*, vol. 18, no. 3, pp. 131–146, 2017.

[3] S. Ito, M. E. Hansen, R. Heiland, A. Lumsdaine, A. M. Litke, and J. M. Beggs, "Extending transfer entropy improves identification of effective connectivity in a spiking cortical network model," *PLoS One*, vol. 6, no. 11, 2011, Art. no. e27431.

[4] O. Stetter, D. Battaglia, J. Soriano, and T. Geisel, "Model-free reconstruction of excitatory neuronal connectivity from calcium imaging signals," *PLoS Comput. Biol.*, vol. 8, no. 8, 2012, Art. no. e1002653.

[5] P. Bonifazi, F. Difato, P. Massobrio, G. L. Breschi, V. Pasquale, T. Levi, M. Goldin, Y. Bornat, M. Tedesco, M. Bisio, S. Kanner, R. Galron, J. Tessadori, S. Taverna, and M. Chiappalone, "In vitro large-scale experimental and theoretical studies for the realization of bi-directional brain-prostheses," *Front. Neural Circuits*, vol. 7, no. March, pp. 1–19, 2013.

[6] H. Lütcke, F. Gerhard, F. Zenke, W. Gerstner, and F. Helmchen, "Inference of neuronal network spike dynamics and topology from calcium imaging data," *Front. Neural Circuits*, vol. 7, no. December, 2013, Art. no. 201.

[7] E. Tibau, M. Valencia, and J. Soriano, "Identification of neuronal network properties from the spectral analysis of calcium imaging signals in neuronal cultures," *Front. Neural Circuits*, vol. 7, 2013, Art. no. 199.

[8] J. G. Orlandi, J. Soriano, E. Alvarez-Lacalle, S. Teller, and J. Casademunt, "Noise focusing and the emergence of coherent activity in neuronal cultures," *Nature Phys.*, vol. 9, no. 9, pp. 582–590, 2013.

[9] J. K. Wrosch, V. V. Einem, K. Breininger, M. Dahlmanns, A. Maier, J. Kornhuber, and T. W. Groemer, "Rewiring of neuronal networks during synaptic silencing," *Sci. Reports*, vol. 7, no. 1, 2017, Art. no. 11724.

[10] L. M. A. Bettencourt, G. J. Stephens, M. I. Ham, and G. W. Gross, "Functional structure of cortical neuronal networks grownin vitro," *Phys. Rev. E*, vol. 75, no. 2, 2007, Art. no. 021915.

[11] A. Maccione, M. Garofalo, T. Nieus, M. Tedesco, L. Berdondini, and S. Martinoia, "Multiscale functional connectivity estimation on low-density neuronal cultures recorded by high-density CMOS micro electrode arrays," *J. Neurosci. Methods*, vol. 207, no. 2, pp. 161–171, 2012.

[12] S. Ito, F.-C. Yeh, E. Hiolski, P. Rydygier, D. E. Gunning, P. Hottowy, N. Timme, A. M. Litke, and J. M. Beggs, "Large-scale, high-resolution multielectrode-array recording depicts functional network differences of cortical and hippocampal cultures," *PLoS One*, vol. 9, no. 8, 2014, Art. no. e105324.

[13] M. Shimono and J. M. Beggs, "Functional clusters, hubs, and communities in the cortical microconnectome," *Cerebral Cortex*, vol. 25, no. 10, pp. 3743–3757, 2014.

[14] M. S. Schroeter, P. Charlesworth, M. G. Kitzbichler, O. Paulsen, and E. T. Bullmore, "Emergence of rich-club topology and coordinated dynamics in development of hippocampal functional networks in vitro," *J. Neurosci.*, vol. 35, no. 14, pp. 5459–5470, 2015.

[15] S. Nigam, M. Shimono, S. Ito, F.-C. Yeh, N. Timme, M. Myroshnychenko, C. C. Lapish, Z. Tosi, P. Hottowy, W. C. Smith, S. C. Masmanidis, A. M. Litke, O. Sporns, and J. M. Beggs, "Rich-club organization in effective connectivity among cortical neurons," *J. Neurosci.*, vol. 36, no. 3, pp. 670–684, 2016.

[16] J. Eckmann, O. Feinerman, L. Gruendlinger, E. Moses, J. Soriano, and T. Tlusty, "The physics of living neural networks," *Phys. Reports*, vol. 449, no. 1–3, pp. 54–76, 2007.

[17] L. J. Millet and M. U. Gillette, "Over a century of neuron culture: From the hanging drop to microfluidic devices," *The Yale J. Biol. Med.*, vol. 85, no. 4, pp. 501–21, 2012.

[18] C. Schmeltzer, J. Soriano, I. M. Sokolov, and S. Rüdiger, "Percolation of spatially constrained Erdös-Rényi networks with degree correlations," *Phys. Rev. E*, vol. 89, no. 1, 2014, Art. no. 012116.

[19] L. Hernández-Navarro, J. G. Orlandi, B. Cerruti, E. Vives, and J. Soriano, "Dominance of metric correlations in two-dimensional neuronal cultures described through a random field ising model," *Phys. Rev. Lett.*, vol. 118, no. 20, pp. 1–5, 2017.

[20] S. Okujeni, S. Kandler, and U. Egert, "Mesoscale architecture shapes initiation and richness of spontaneous network activity," *J. Neurosci.*, vol. 37, no. 14, pp. 3972–3987, 2017.

[21] M. Barthélemy, "Spatial networks," *Phys. Reports*, vol. 499, no. 1–3, pp. 1–101, 2011.

[22] G. Bianconi, P. Pin, and M. Marsili, "Assessing the relevance of node features for network structure," *Proc. Nat. Acad. Sci. United States America*, vol. 106, no. 28, pp. 11 433–11 438, 2009.

[23] D. Brockmann and D. Helbing, "The hidden geometry of complex, network-driven contagion phenomena," *Sci.*, vol. 342, no. 6164, pp. 1337–1342, 2013.

[24] S. Horvát, R. Gamanut, M. Ercsey-Ravasz, L. Magrou, B. Gamanut, D. C. Van Essen, A. Burkhalter, K. Knoblauch, Z. Toroczkai, and H. Kennedy, "Spatial embedding and wiring cost constrain the functional layout of the cortical network of rodents and primates," *PLoS Biol.*, vol. 14, no. 7, 2016, Art. no. e1002512.

[25] M. Jacomy, T. Venturini, S. Heymann, and M. Bastian, "ForceAtlas2, a continuous graph layout algorithm for handy network visualization designed for the gephi software," *PLoS One*, vol. 9, no. 6, 2014, Art. no. e98679.

[26] S. Teller, C. Granell, M. De Domenico, J. Soriano, S. Gómez, and A. Arenas, "Emergence of assortative mixing between clusters of cultured neurons," *PLoS Comput. Biol.*, vol. 10, no. 9, 2014, Art. no. e1003796.

[27] T. Opitz, A. D. De Lima, and T. Voigt, "Spontaneous development of synchronous oscillatory activity during maturation of cortical networks in vitro," *J. Neurophysiol.*, vol. 88, no. 5, pp. 2196–2206, 2002.
[28] D. Wagenaar, J. Pine, and S. Potter, "An extremely rich repertoire of bursting patterns during the development of cortical cultures," *BMC Neurosci.*, vol. 7, no. 1, 2006, Art. no. 11.
[29] D. J. Watts and S. H. Strogatz, "Collective dynamics of 'small-world' networks," *Nature*, vol. 393, no. 6684, pp. 440–442, 1998.
[30] A. Fronczak, P. Fronczak, and J. A. Hołyst, "Average path length in random networks," *Phys. Rev. E*, vol. 70, no. 5, 2004, Art. no. 7.
[31] J. Soriano, M. R. Martínez, T. Tlusty, and E. Moses, "Development of input connections in neural cultures," *Proc. Nat. Acad. Sci. United States America*, vol. 105, no. 37, pp. 13 758–13 763, 2008.
[32] S. Jacobi, J. Soriano, M. Segal, and E. Moses, "BDNF and NT-3 increase excitatory input connectivity in rat hippocampal cultures," *Eur. J. Neurosci.*, vol. 30, pp. 998–1010, 2009.
[33] F. D. V. Fallani, M. Corazzol, J. Sternberg, C. Wyart, and M. Chavez, "Hierarchy of neural organization in the embryonic spinal cord: Granger-causality graph analysis of calcium imaging data," *IEEE Trans. Neural Syst. Rehabil. Eng.*, vol. 23, no. 3, pp. 333–341, May 2015.
[34] J. G. Orlandi, O. Stetter, J. Soriano, T. Geisel, and D. Battaglia, "Transfer entropy reconstruction and labeling of neuronal connections from simulated calcium imaging," *PLoS One*, vol. 9, no. 6, 2014, Art. no. e98842.
[35] O. Cohen, A. Keselman, E. Moses, M. Rodríguez Martínez, J. Soriano, and T. Tlusty, "Quorum percolation in living neural networks," *Europhys. Lett.*, vol. 89, no. 1, 2010, Art. no. 18008.
[36] D. Lonardoni, H. Amin, S. Di Marco, A. Maccione, L. Berdondini, and T. Nieus, "Recurrently connected and localized neuronal communities initiate coordinated spontaneous activity in neuronal networks," *PLoS Comput. Biol.*, vol. 13, no. 7, 2017, Art. no. e1005672.
[37] S. Teller, I. B. Tahirbegi, M. Mir, J. Samitier, and J. Soriano, "Magnetite-amyloid-$\beta$ deteriorates activity and functional organization in an in vitro model for Alzheimer's disease," *Sci. Reports*, vol. 5, no. 1, pp. 1–16, 2015.
[38] E. Alvarez-Lacalle and E. Moses, "Slow and fast pulses in 1-D cultures of excitatory neurons," *J. Comput. Neurosci.*, vol. 26, no. 3, pp. 475–493, 2009.
[39] E. M. Izhikevich, *Dynamical Systems in Neuroscience*. Cambridge, MA, USA: MIT Press, 2007.
[40] E. Izhikevich, "Simple model of spiking neurons," *IEEE Trans. Neural Netw.*, vol. 14, no. 6, pp. 1569–1572, Nov. 2003.
[41] D. Golomb and Y. Amitai, "Propagating neuronal discharges in neocortical slices: Computational and experimental study," *J. Neurophysiol.*, vol. 78, no. 3, pp. 1199–1211, 1997.
[42] D. Cohen and M. Segal, "Network bursts in hippocampal microcultures are terminated by exhaustion of vesicle pools," *J. Neurophysiol.*, vol. 106, no. 5, pp. 2314–2321, 2011.
[43] L. F. Abbott, "Synaptic depression and cortical gain control," *Sci.*, vol. 275, no. 5297, pp. 221–224, 1997.
[44] W. Mader, M. Mader, J. Timmer, M. Thiel, and B. Schelter, "Networks: On the relation of bi- and multivariate measures," *Sci. Reports*, vol. 5, no. 1, 2015, Art. no. 10805.
[45] T. Schreiber, "Measuring information transfer," *Phys. Rev. Lett.*, vol. 85, no. 2, pp. 461–464, 2000.
[46] W. Li, "Mutual information functions versus correlation functions," *J. Statisiical Phys.*, vol. 60, no. 5/6, pp. 823–837, 1990.
[47] J. G. Orlandi, O. Stetter, J. Soriano, T. Geisel, and D. Battaglia, "Transfer entropy reconstruction and labeling of neuronal connections from simulated calcium imaging," *PLoS One*, vol. 9, no. 6, 2014, Art. no. e98842.
[48] J. M. Beggs and D. Plenz, "Neuronal avalanches are diverse and precise activity patterns that are stable for many hours in cortical slice cultures," *J. Neurosci.*, vol. 24, no. 22, pp. 5216–5229, 2004.
[49] G. Fagiolo, "Clustering in complex directed networks," *Phys. Rev. E*, vol. 76, no. 2, 2007, Art. no. 026107.
[50] M. E. J. Newman, "Assortative mixing in networks," *Phys. Rev. Lett.*, vol. 89, no. 20, 2002, Art. no. 208701.
[51] B. Efron, "Computers and the theory of statistics: Thinking the unthinkable," *SIAM Rev.*, vol. 21, no. 4, pp. 460–480, 1979.

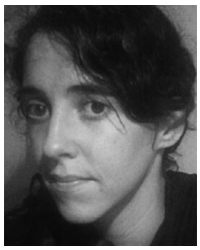

**Elisenda Tibau** received the MSc degree in biophysics and a PhD degree in physics from the University of Barcelona, Spain. Her research focuses in the modeling of spontaneous activity in neuronal cultures using linear and nonlinear approaches, and combining experiments with numerical simulations. She also investigates the relation between the structural and the effective connectivities in neuronal networks.

**Adriaan Alexander Ludl** received the PhD degree in chemical physics from Université Pierre et Marie Curie, Paris, France. He is currently a postdoctoral researcher with the University of Barcelona, Spain. His research interests include living neuronal networks, inference of network structure and the modeling of their dynamics. He is involved in the development of network inference algorithms for living neuronal tissues within the MESO-BRAIN project.

**Sten Rüdiger** received the diploma degree in mathematics from Free University Berlin, Germany, and a PhD degree in nonlinear science from University Potsdam, Germany. He is currently working with the Department of Physics, Humboldt University at Berlin, Germany. His research includes the dynamics of calcium ions in cells as well as the investigation of calcium channels in neuronal synapses. He also works on various aspects of network science and applications to epidemics and neural behavior.

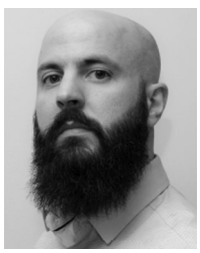

**Javier G. Orlandi** received the MSc degree in biophysics and the PhD degree in physics from the University of Barcelona, where he developed in silico models to generate realistic neuronal networks embedded in metric spaces. He is currently postdoctoral fellow with the University of Calgary, where he works in the development of novel techniques to assess the activity and connectivity of neuronal networks from calcium imaging experiments.

**Jordi Soriano** received the PhD degree in physics from the University of Barcelona, Spain. He was then research fellow with the University of Bayreuth, Germany and the Weizmann Institute of Science, Israel, where he studied multicellular organization and connectivity in neuronal cultures. He is currently associate professor with the University of Barcelona. His research covers the understanding of spontaneous activity in neuronal cultures and the relation between structural and effective connectivity, both in health and disease.